Geophysical Journal International

Geophys. J. Int. (2018) **214,** 1206–1217
Advance Access publication 2018 May 18
GJI Marine geosciences and applied geophysics

doi: 10.1093/gji/ggy196

Frequency-depth-dependent spherical reflection response from the sea surface — a transmission experiment

Daniel Wehner,[1] Martin Landrø,[2] Lasse Amundsen[1,3] and Harald Westerdahl[3]

[1]*Department of Geoscience and Petroleum, NTNU,* 7031 *Trondheim, Norway. E-mail: daniel.wehner@ntnu.no*
[2]*Department of Electronic Systems, NTNU,* 7491 *Trondheim, Norway*
[3]*Statoil Research Centre,* 7053 *Trondheim, Norway*

Accepted 2018 May 17. Received 2018 January 19; in original form 2018 April 27

SUMMARY

In academia and the industry, there is an increasing interest in generating and recording low seismic frequencies, which lead to better data quality, deeper signal penetration and can be important for full-waveform inversion. The common marine seismic source in acquisition is the air gun which is towed behind a vessel. The frequency content of the signal produced by the air gun mainly depends on its source depth as there are two effects that are presumed to counteract each other. First, there is the oscillating air bubble generated by the air gun that leads to more low frequencies for shallow source depths. Second, there is the interference of the downgoing wave with the first reflection from the sea surface, referred to as the ghost, which leads to more low frequencies for deeper source depths. It is still under debate whether it is beneficial to place the source shallow or deep to generate the strongest signal for frequencies below 5 Hz. Therefore, the ghost effect is studied in more detail by measuring the transmission at the water–air interface. We conduct experiments in a water tank where a small-volume seismic source is fired at different depths below the water surface to investigate how the ghost varies with frequency and depth. The signal from the seismic source is recorded with hydrophones inside water and air during the test to estimate the transmitted signal through the interface. In a second test, we perform experiments with an acoustic source located in air that is fired at different elevations above the water surface. The source in air is a starter gun and the signals are again recorded in water and air. The measured data indicate an increasing transmission of the signal through the water–air interface when the source is closer to the water surface which leads to a decreasing reflection for sources close to the surface. The measured results are compared with modelled data and the existing theory. The observed increase in transmission for shallow source depths could be explained by the theory of a spherical wave front striking the interface instead of assuming a plane wave front. The difference can be important for frequencies below 1 Hz. The results suggest that deploying a few sources very shallow during marine seismic acquisition could be beneficial for these very low frequencies. In addition, the effect of a spherical wave front might be considered for modelling far-field signatures of seismic sources for frequencies below 1 Hz.

Key words: Acoustic properties; Controlled source seismology; Seismic instruments; Wave scattering and diffraction.

1 INTRODUCTION

The almost perfect reflection of acoustic waves at the water–air interface is a well-known effect in many applications. In seismic acquisition, the first reflection from the sea surface that follows the downgoing source signal is referred to as the ghost, which is a main problem for generating low frequencies. The signal created by a single marine seismic source like the air gun or water gun propagates spherically in all directions. Due to the short time delay, the ghost reflection is overlapping with the downgoing wavefield. This leads to unwanted effects as certain frequencies vanish due to destructive interference depending on the source depth. Especially, low frequencies approaching 0 Hz are thought to vanish completely due to the ghost. This assumption is correct for a reflection coefficient of −1 which is independent of frequency and source depth. In practice this approximation often seems to be sufficient. However, a more detailed description of the reflection from the sea surface depending

on source depth and frequency could lead to new considerations in seismic acquisition and better processing of seismic data.

There are several effects that can have an impact on the ghost reflection. First, the source signature can vary due to interaction between the source and an interface like the sea surface. The impact on cavities or air bubbles close to the water surface was studied by several authors on small scales, mostly in the range of millimetres. Chahine (1977) and Blake & Gibson (1981) performed experiments with electrodes to create cavities near the water–air interface. They conclude on a distance between the cavity and interface within the cavity is interacting with the boundary. This happens when the cavity–interface distance is less than three times the maximum radius of the cavity. A numerical study of the interaction between a bubble and the water–air interface is illustrated by Wang *et al.* (1996). For seismic sources, there are studies on the interaction of air bubbles in clustered air gun arrays when they are close to each other (Strandenes & Vaage 1992). Due to these interactions, the source signature is changing (Giles & Johnston 1973) as neighbouring source bubbles act as a boundary. The changing bubble time period caused by the interaction of clustered guns is demonstrated by Barker & Landrø (2012).

Second, the reflection coefficient can vary due to the shape and properties of the interface itself. The changing reflection coefficient for different surface topographies, due to wind and weather, is described in theory by many authors (Brekhovskikh & Lysanov 1991; Hovem 2007; Jensen *et al.* 2011). This weather effect mainly has an impact on high seismic frequencies as demonstrated by Kryvohuz & Campman (2017). Klüver & Tabti (2015) illustrate how the reflection coefficient could be estimated from dual-sensor streamer data. Additionally, recent theoretical analyses demonstrate that a monopole sound source would radiate more acoustic energy into air than expected if the source depth is much less than the emitted acoustic wavelength (Godin 2006; McDonald & Calvo 2007; Godin 2008; Glushkov *et al.* 2013). This phenomenon is caused by the evanescent component of the wave inside water which can be converted to a homogeneous wave inside air for specific wavenumbers. Calvo *et al.* (2013) and Voloshchenko & Tarasov (2013) conducted acoustic experiments using sound sources ranging from 1 to 20 kHz and they verified the increased signal transmission from water to air for shallow source depths relative to the wavelength. Another theoretical study by Deng *et al.* (2012) illustrates a similar effect for a moving point source underwater. Therefore, it might be possible to use recorded sound in air emitted from marine seismic sources to measure properties of the atmosphere.

Third, an almost perfect, frequency-independent reflection coefficient is based on the assumption of plane wave propagation. However, marine seismic sources emit spherical waves that cause a frequency- and depth-dependent reflection as shown by Brekhovskikh & Lysanov (1991) and Aki & Richards (2002). The spherical reflection response deviates most from the plane wave reflection coefficient for low frequencies, or more precisely for wavelength larger than the source–interface distance. This effect is demonstrated by Li *et al.* (2017a), Li *et al.* (2017b) and Yan *et al.* (2017) for amplitude versus offset analysis of seismic data between two acoustic media.

This research opens up on the question if the reflected signal from the surface decreases for shallow source depths relative to the emitted wavelength. If this is the case, the destructive interference within the low-frequency range between the initially downgoing wavefield and ghost reflection is less than in a model of a constant reflection coefficient close to -1 and that would be beneficial for generating low frequencies. Recently presented experimental results from Amundsen *et al.* (2017) indicate an increased low-frequency signal for shallow large-volume single-gun sources. We conduct experiments in a water tank to measure the transmitted signal from sources at varying distances to the water–air interface. We focus on the transmission and reflection from a source placed in water. In addition, a second experiment with a source in air is conducted. The transmission from air to water is discussed by many authors in ocean acoustics for large ranges (Hudimac 1957; Young 1973; Lubard & Hurdle 1976). The sources are placed in water and air to investigate the transmission from both sides of the interface. The experimental results should provide a better understanding of the transmitted and reflected signal when the source is fired close to the sea surface and hence the depth is small compared to the acoustic wavelength. We compare the reflection from the sea surface assuming models for plane and spherical waves. The change of the reflected signal within the low-frequency band is of special interest.

2 THEORY

We are interested in the transmitted and reflected signal at the water–air interface and how this might change with source depth and frequency. Therefore, the plane wave reflection coefficient and spherical wave reflection response for a flat interface between two acoustic media are compared (Fig. 1).

Plane waves are characterized by a constant phase and amplitude on the plane that is perpendicular to the direction of propagation (Kinsler *et al.* 1962). These planes are indicated as lines in 2-D in Fig. 1 (bottom). From this assumption, the plane wave reflection and transmission coefficients at a flat fluid–fluid interface are defined as (Kinsler *et al.* 1962)

$$R_{\mathrm{pp}} = \frac{\rho_2 c_2/\cos(\theta_2) \; - \; \rho_1 c_1/\cos(\theta_1)}{\rho_2 c_2/\cos(\theta_2) \; + \; \rho_1 c_1/\cos(\theta_1)}, \tag{1}$$

$$T_{\mathrm{pp}} = \frac{2\;\rho_2 c_2/\cos(\theta_2)}{\rho_2 c_2/\cos(\theta_2) \; + \; \rho_1 c_1/\cos(\theta_1)}, \tag{2}$$

where ρ_i and c_i with $i = 1, 2$, denote the density and velocity of the respective layer (Fig. 1). The incident and reflected angles are indicated by θ_1 and θ_2 is the angle of refraction where θ_2 can be computed following Snell's law as (Huygens 1690)

$$\theta_2 = \arcsin\Big(\frac{c_2 \sin(\theta_1)}{c_1}\Big). \tag{3}$$

At the water–air interface changes of the reflection and transmission coefficient for varying angles θ_1 are small, ranging from $R_{\mathrm{pp}} = -0.9994$ at $\theta_1 = 0^\circ$ to $R_{\mathrm{pp}} = -1$ at $\theta_1 = 90^\circ$. The relation between reflection and transmission for a flat surface can be written as

$$R_{\mathrm{pp}} = T_{\mathrm{pp}} - 1. \tag{4}$$

Spherical waves that are incident and reflected from an interface can be expressed as the superposition of cylindrical waves following Sommerfeld's integral (Aki & Richards 2002). The spherical wave reflection response at a flat fluid–fluid interface can be described as the ratio between the reflected and incident wave and is given as (Ursenbach & Haase 2006; Li *et al.* 2017a)

$$R_{\mathrm{sph}} = \frac{\int_1^0 R_{\mathrm{pp}}(x)\Psi \,\mathrm{d}x + i\int_0^\infty R_{\mathrm{pp}}(ix)\Phi \,\mathrm{d}x}{\int_1^0 \Psi \,\mathrm{d}x + i\int_0^\infty \Phi \,\mathrm{d}x}, \tag{5}$$

$$\Psi = J_0(\omega r\sqrt{1-x^2}/c_1)\mathrm{e}^{(i\omega x(z_{\mathrm{r}}+z_{\mathrm{s}})/c_1)}, \tag{6}$$

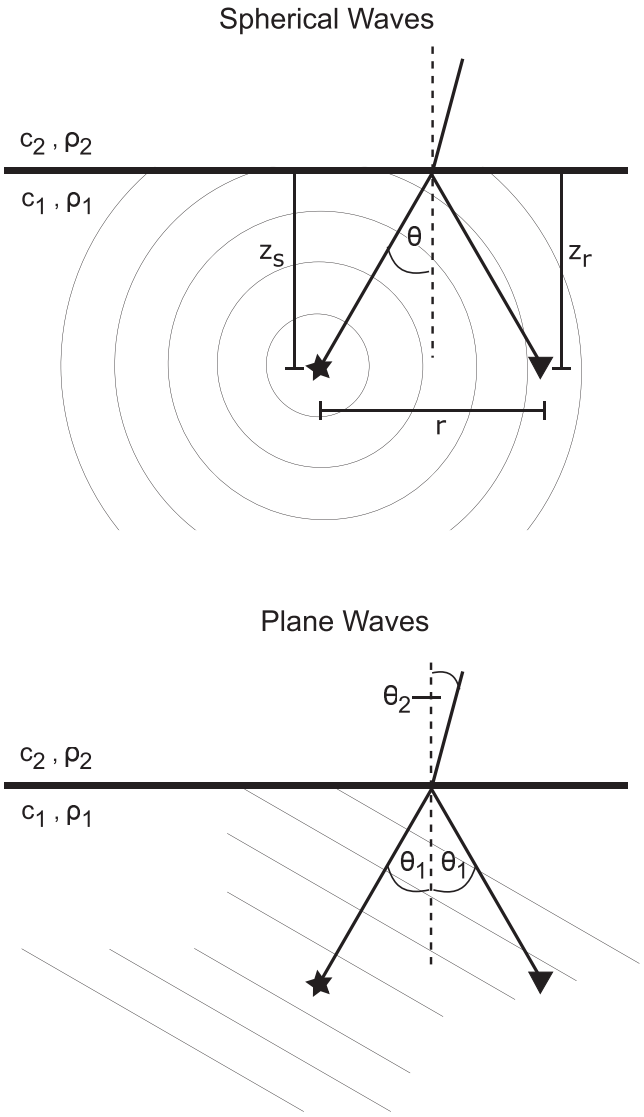

Figure 1. Spherical wave incident on a flat interface and important parameters for the computation of R_{sph} (top). Plane wave incident on a flat interface and important parameters for the computation of R_{pp} (bottom).

$$\Phi = J_0(\omega r\sqrt{1+x^2}/c_1)\mathrm{e}^{(-\omega x(z_\mathrm{r}+z_\mathrm{s})/c_1)}, \tag{7}$$

where ω is the angular frequency, r is the horizontal offset between source and receiver, while z_r and z_s are the receiver–interface and source–interface distance, respectively (Fig. 1, top). The integration variable is $x = \cos(\theta_1)$ and J_0 is the zero-order Bessel function. As it depends also on the source and receiver depth and not only on the medium parameters, the spherical wave reflection is defined as a response rather than a coefficient. The same relation as in eq. (4) can be used to obtain the reflection response from measured transmitted signals

$$R_{\mathrm{sph}} = T_{\mathrm{sph}} - 1. \tag{8}$$

We note that the plane wave reflection coefficient R_{pp} changes only with angle of incidence, whereas the spherical wave reflection response R_{sph} depends on the incident angle, frequency, source and receiver depths. The difference between both equations is illustrated in Fig. 2 for varying frequencies and source depths. For the computation, we use $v_1 = 1500$ m s^{-1}, $\rho_1 = 1000$ kg m^{-3} for the parameters of water and $v_2 = 340$ m s^{-1}, $\rho_2 = 1.25$ kg m^{-3} for

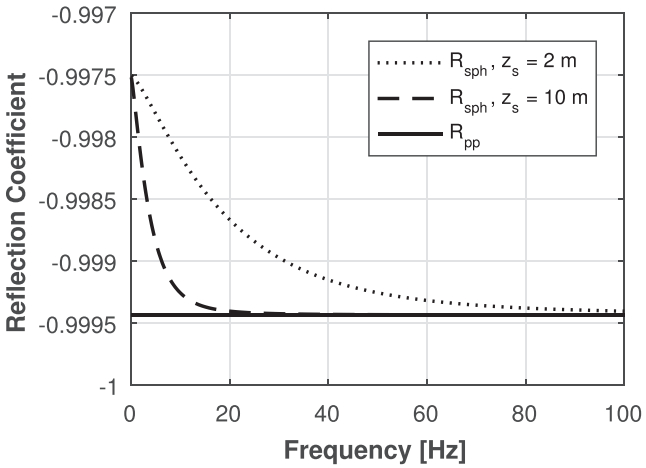

Figure 2. Plane wave reflection coefficient (solid line) and spherical wave reflection response for two different source depths (dotted and dashed line) at the water–air interface as a function of frequency.

those in air. We assume that the source and receiver depths are the same as the seismic source is so close to the water–air interface, that the ghost reflection is an inherent part of the source signature. Although the difference is small, the question remains if it can be recognized on measured data.

3 EXPERIMENTS

Two experiments are conducted to investigate the impact on the reflected and transmitted signal in relation to source depth and frequency. We perform a first experiment where a source is fired in water (A) and a second one where a source is fired in air (B). All experiments are performed in a water tank with a length of 6 m, a width of 2.5 m and a depth of 1.4 m, respectively (Fig. 3a). The walls of the tank are equipped with 5 cm thick foam mattresses. Although they do not act as perfectly absorbing boundaries, previous tests showed an improved signal reception with smaller side reflections. For both experiments different receiver geometries are used to investigate the dependence of the transmitted signal on the source depth and incident angle on the water–air interface. Brüel & Kjær hydrophones of the type 8105 are used as receivers which have a frequency range from 0.1 Hz to 100 kHz. The hydrophones have the same sensitivity in water and air up to a frequency of 3 kHz. Therefore, we use the same hydrophones to record the signal in air. Due to the fact that we use strong sources, the lower sensitivity compared to microphones is not an issue for our experiment. The receivers are not coupled to the tank during the experiments to avoid impacts on the measured low frequencies.

3.1 Experiment A: source in water

The source is a S15 water gun with one cylindrical gun port that is built for borehole applications (Fig. 3b). The gun has a volume of 15 in^3 (*ca.* 0.25 l) for the water chamber as indicated by the model number S15. The water gun generates a high velocity water jet when the water is pushed out from the gun chamber. Due to the high velocity, a cavity is created which collapses when the water jet slows down. The cylindrical gun port shape allows us to generate a cavity at a quite accurate position compared to the common radial gun ports with several openings. For more details on the water gun the reader is referred to Landrø *et al.* (1993).

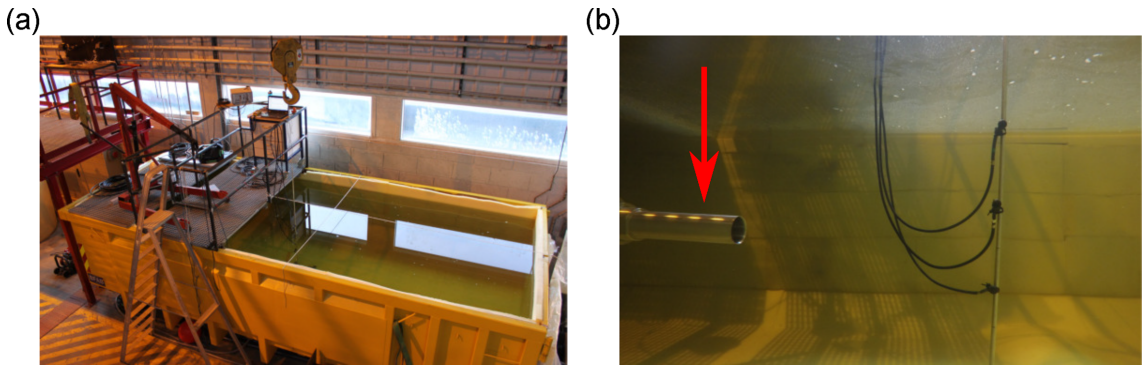

Figure 3. (a) Photo of the water tank with dimensions 6 m × 2.5 m × 1.4 m. (b) Underwater photo with gun port of water gun on the left side (red arrow) and hydrophones in the middle.

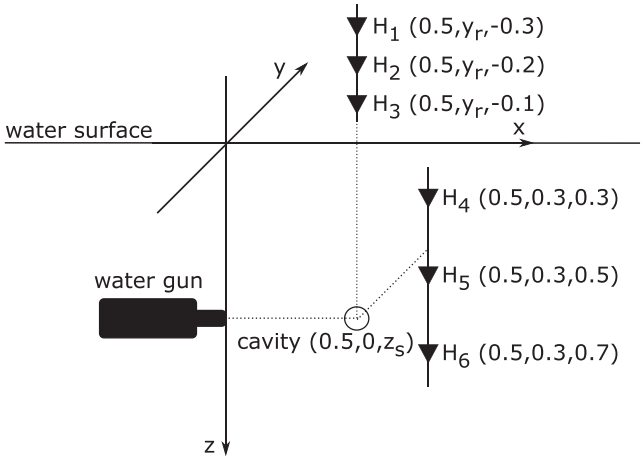

Figure 4. Schematic sketch of the experimental setup using the water gun as a source in water. Numbers in brackets indicate the coordinates (x,y,z) in metres.

We conduct one experiment to investigate the impact of source depth on the vertically transmitted signal. A second experiment is performed where the receivers in air are moved to different offsets to investigate the impact of incident angle on the transmitted signal. The experimental setups are as follows:

(1) First, three hydrophones are located vertically above the estimated location of the cavity in air with a distance of $z_r = -0.3$, -0.2 and -0.1 m to the water–air interface, while $y_r = y_s = 0$. We denote these hydrophones as H1, H2 and H3 (Fig. 4). Then the water gun is fired three times at different source depths z_s, ranging from 0.2 to 0.8 m with an increment of 0.1 m. Afterwards, the same experiment is repeated while the three hydrophones are located inside the water at depths of $z_r = 0.3$, 0.5, 0.7 m and a horizontal offset of $y_r = 0.3$ m between the cavity and receiver. We denote these hydrophones as H4, H5 and H6 (Fig. 4). The offset in x-direction is estimated to be the same for the source and receivers which means $x_r = x_s$. This is the best acquisition we could get due to practical considerations in the laboratory.

(2) For the second test, the source depth is constant at $z_s = 0.3$ m and the position of hydrophones H4, H5 and H6 is the same as in the first experiment. The receivers H1, H2 and H3 are moved to different y_r positions, ranging from 0 to 0.6 m with an increment of 0.1 m, while x_r and z_r are also constant. For each receiver position the source is fired three times.

3.2 Experiment B: source in air

The source is a Stalker R1 2.5″ gun that has a caliber of 0.38 in. (9 mm) and blank bullets, which for instance is used in athletics. The propellant of the bullet has a weight of 0.56 g and a caloric equivalent of 3.06 kJ g^{-1} which leads to a released energy of approximately 1.71 kJ for one blank bullet. The signalgun is fixed to the metal frame of the tank above the water surface and a near-field hydrophone is attached to it (Fig. 5a). The near-field hydrophone is used to measure the source signature and trigger the recording during the experiments. Similar to experiment A, we conducted a test to investigate the impact of source elevation on the vertically transmitted signal. The experimental setup is as follows:

(1) One hydrophone is placed inside water at a depth of $z_r = 0.05$ m indicated by H1. The second hydrophone, H2, is located in air at $z_r = -0.05$ m (Fig. 6). They are both located at $x_r = y_r = 0$ m. The signalgun is also placed at $x_s = y_s = 0$ m. During this test the source is moved to different elevations z_s, ranging from -0.2 to -0.8 m with an increment of -0.1 m. At each source position, the signalgun is fired four times.

3.3 Source signature and repeatability

For the later estimation of the transmitted signal, the maximum amplitudes of the signal recorded in water and air are compared. Therefore, the source signatures and their repeatability are investigated.

Fig. 7 illustrates the signal recorded in water and air which is created by the water gun in experiment A for different frequency bands. The signature is characterized by a small positive peak between 0.01 and 0.02 s when the water is pushed out of the gun chamber, followed by a negative peak due to the growing cavity. The main peak around 0.04 s is created by the collapse of the cavity. A second peak at 0.053 s can be recognized which is due to an oscillation of the cavity. The photos in Fig. 7 illustrate the shape of the water jet at different times after the water gun is fired while the cavity is difficult to identify from these pictures. The water jet velocity can be roughly estimated from the pictures which leads to an averaged value of 30 m s^{-1}. For the lowest frequencies (Fig. 7, top) both signals have almost the same shape, indicating that we can record the same signal in air and water. The time difference between both recordings fits to the source–receiver distance and the slower sound velocity in air compared to water. The phase within the different frequency bands is shifted due to the applied filter while the amplitude is unaffected which is important for our investigation. We

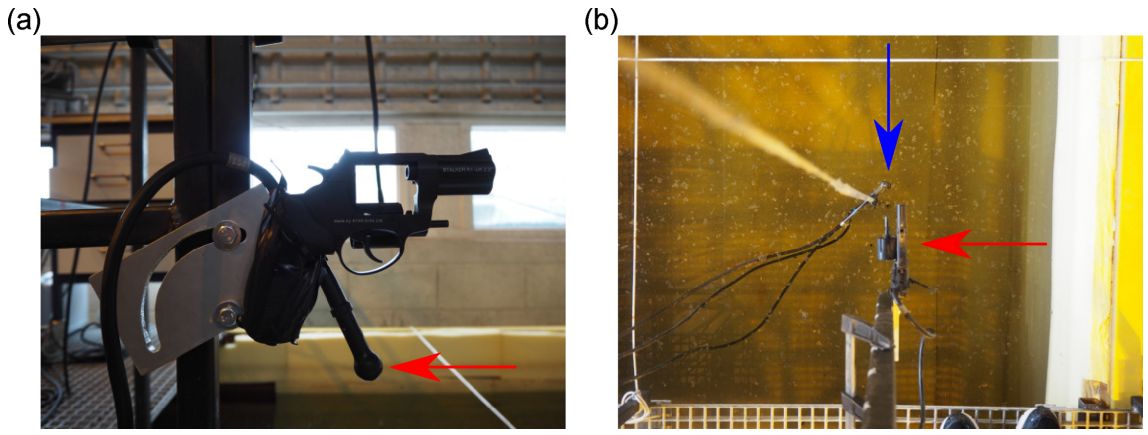

Figure 5. (a) Photo of the signalgun and near-field hydrophone indicated by red the arrow. (b) Top view of the experimental setup with signalgun (red arrow) and hydrophones (blue arrow).

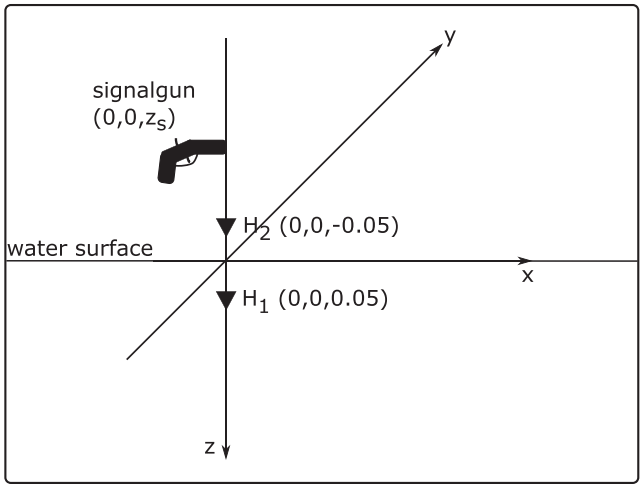

Figure 6. Schematic sketch of the experimental setup using the signalgun as a source in air. Numbers in brackets indicate the coordinates (*x,y,z*) in metres.

note that including higher frequencies in the signal (Fig. 7, bottom) leads to more deviations between the signal in water and air which can be observed around 0.04 and 0.06 s.

As the signal in water and air is not recorded at the same time during experiment A, the repeatability of the source signal is important. Therefore, we compare the relative difference of the maximum amplitude for one hydrophone *Hi* between repeated shots at the same depth as

$$\delta A(Hi) = \frac{\Delta A_{\max}(Hi)}{A_{\max}(Hi)} \times 100, \tag{9}$$

where $A_{\max}(Hi)$ is the mean maximum amplitude recorded at one hydrophone while $i = 1, 2, 3$ for the receivers in air and $i = 4, 5, 6$ for the receivers in water, respectively. The mean difference of the maximum amplitude between each repeated shot at the same depth is $\Delta A_{\max}(Hi) = |A^n_{\max}(Hi) - A^m_{\max}(Hi)|$ where $n = m = 1, 2, 3$ indicate the shot number at each source depth z_s. The difference $\Delta A_{\max}(Hi)$ is computed for all combinations of n and m, except for $n = m$. Then the mean value of all hydrophones in air is calculated as

$$\mu(\delta A) = \frac{1}{N}\sum_{i=1}^{N} \delta A(Hi), \tag{10}$$

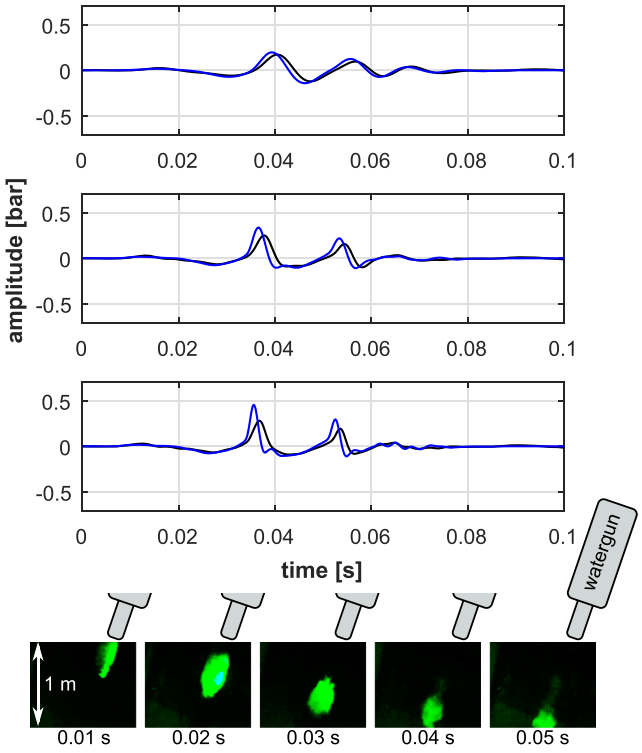

Figure 7. Recorded signal at hydrophone H2 in air (black) and H5 in water (blue) according to Fig. 4. The signal of H2 in air is multiplied by a factor of 250. The source was fired at $z_s = 0.3$ m. The signal is filtered with a 10–100 Hz (top), 10–200 Hz (middle) and 10–300 Hz (bottom) bandpass filter. Photos show a top view of the created water jet while the water gun is fired according to different times. The position of the water gun is sketched.

where N is the total number of hydrophones which is three in our case. The same is repeated for the measurements in water and the results for each source depth are illustrated in Fig. 8. It should be noted that the repeatability is better for deeper source depths as the cavity created near the surface is within the minimum operation depth of the water gun. The important aspect is that amplitude changes between repeated shots are less than changes due to varying source depth.

Fig. 9 illustrates the signal recorded in water and air which is created by the signalgun in experiment B for different frequency bands. The signature is characterized by a main positive peak around

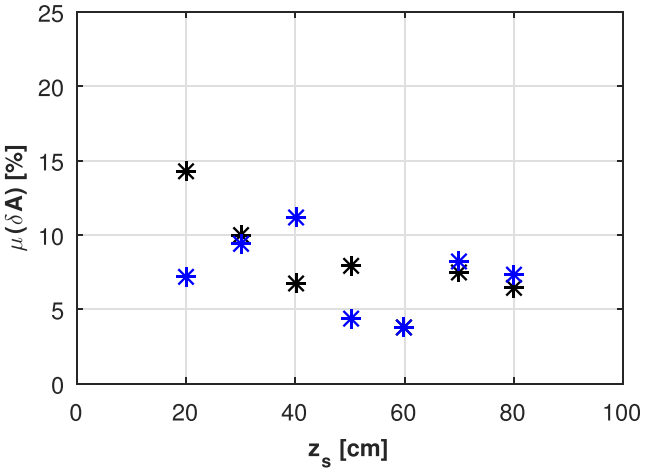

Figure 8. Relative difference $\mu(\delta A)$ between the mean maximum recorded amplitude and the difference amplitude between repeated shots for the signal filtered within 10–100 Hz for experiment A. For the hydrophones in air (black) and water (blue).

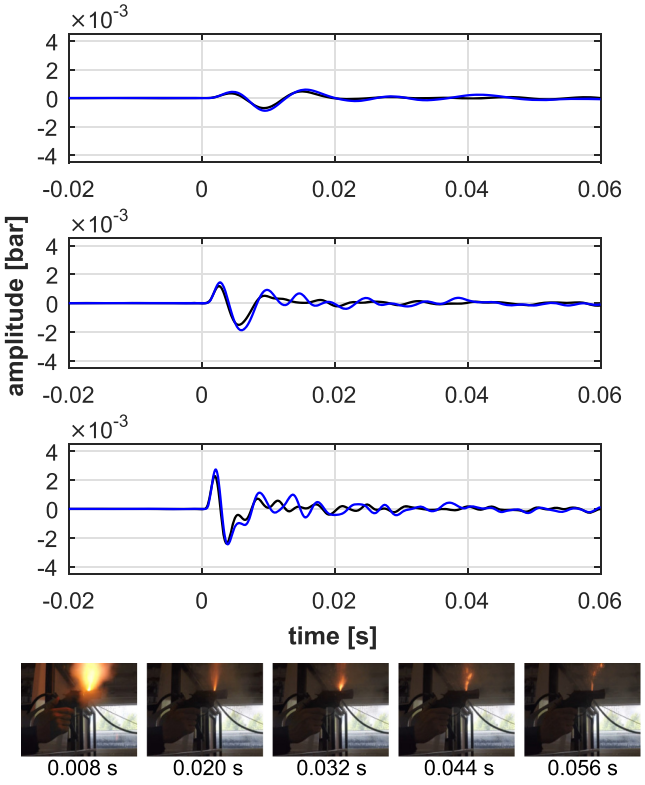

Figure 9. Recorded signal at hydrophone H2 in air (black) and H1 in water (blue) according to Fig. 6. The source was fired at $z_s = -0.3$ m. The signal is filtered with a 10–100 Hz (top), 10–200 Hz (middle) and 10–300 Hz (bottom) bandpass filter. Photos show a side view of the signalgun while it is fired according to different times.

0.004 s which is caused by the firing of the signalgun. This can be seen on the photos taken during the shot (Fig. 9). It should be mentioned that the photos and pressure recordings are not synchronized and hence there could be small deviations in time. The signal after the main peak could be caused by reverberations of the signalgun. Although the signal is weak for the lowest frequency range, the shape of the main peak is similar for all plots (Fig. 9), again indicating that we can record the same signal in air and water. The small time difference between both peaks fits to the source–receiver distance and the slower sound velocity in air compared to water. For higher frequencies, deviations between the signal in water and air are strongly pronounced, especially after the main peak. However, we only consider the main peak for further investigations of the transmitted signal.

During experiment B, the receivers are placed in water and air at the same time while the source is fired. Therefore, the repeatability investigation is not relevant. However, the radiation pattern of the signalgun is assumed to be more complex than a collapsing cavity. Therefore, we measure the radiation pattern of the signalgun in different planes (x–z and x–y) according to our experimental setup (Fig. 6). We conclude that the signal emitted below the z_s–x plane in which the signalgun is located is similar in all directions.

4 MODELLING

A modelling study is conducted to compare the measured results with modelled data and to investigate the impact of the tank dimensions on the experimental results. We simulate the data solving the 3-D Helmholtz equation in a finite element scheme using the Comsol software. The maximum frequency of investigation is $f_{max} = 300$ Hz and the minimum velocity in the model is $v_{min} = 340$ m s^{-1}, leading to a minimum wavelength of $\lambda_{min} = 1.13$ m. A minimum of $n = 8$ mesh elements per wavelength and a time step of $t_{step} = 1.25\text{e}{-4}$ s is used which indicates a Courant–Friedrichs–Lewy number of 0.3 (Courant *et al.* 1928). These parameters reveal a stable and accurate simulation in our case. As input source an averaged, measured near-field source signature is implemented where the mean measured water gun signal from all experiments A is computed and filtered to the frequency range of investigation. The same is done for the modelling of experiment B where the source is in air. Therefore, the source depth and receiver offsets are the only parameters that change during the modelling according to the experimental setup. As we are mainly investigating the ratio between the maximum amplitude of the signal in air and water, this is an adequate approximation of the source.

An important issue for the experimental results is the limited size of the water tank. Although damping material is placed at the walls, side reflections will have a small impact on the measured data. Therefore, we simulate the transmitted signal within three different settings:

(1) Tank model: compute the transmission within a tank model according to the experimental setup. The 3-D tank model consists of the metal tank, a foam layer, the water and a surrounding air medium.

(2) Free-field model: compute the transmission for a two-layer medium (water and air) without any tank boundaries using the same acquisition geometry as in the experiment.

(3) Homogeneous model: compute the wave propagation within a homogeneous (either water or air) medium using the same acquisition geometry as in the experiment.

The modelled results of all three settings at one receiver position are illustrated in Fig. 10(a) for experiment A and in Fig. 10(b) for experiment B. It should be noted that the results from the homogeneous model are close to the source input as the signatures are only influenced by geometrical spreading. There are small differences between the tank and free-field model which are caused by the limited size of our water tank. They are considered to be negligible as

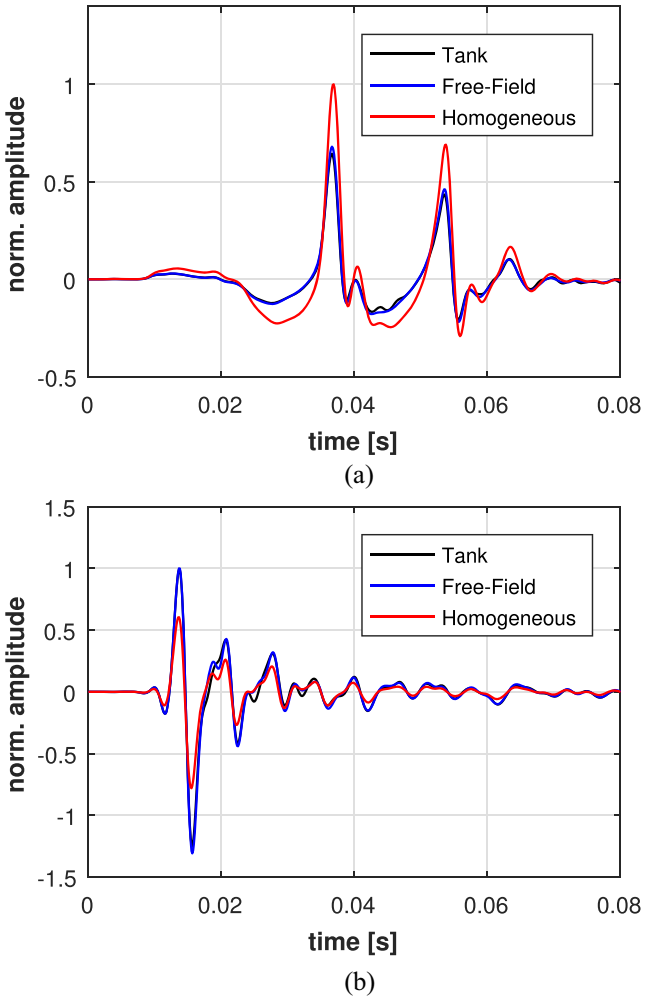

Figure 10. (a) Modelled results at receiver H5 (Fig. 4) for three different settings using the water gun signature. (b) Modelled results at receiver H2 (Fig. 6) for three different settings using the signalgun signature.

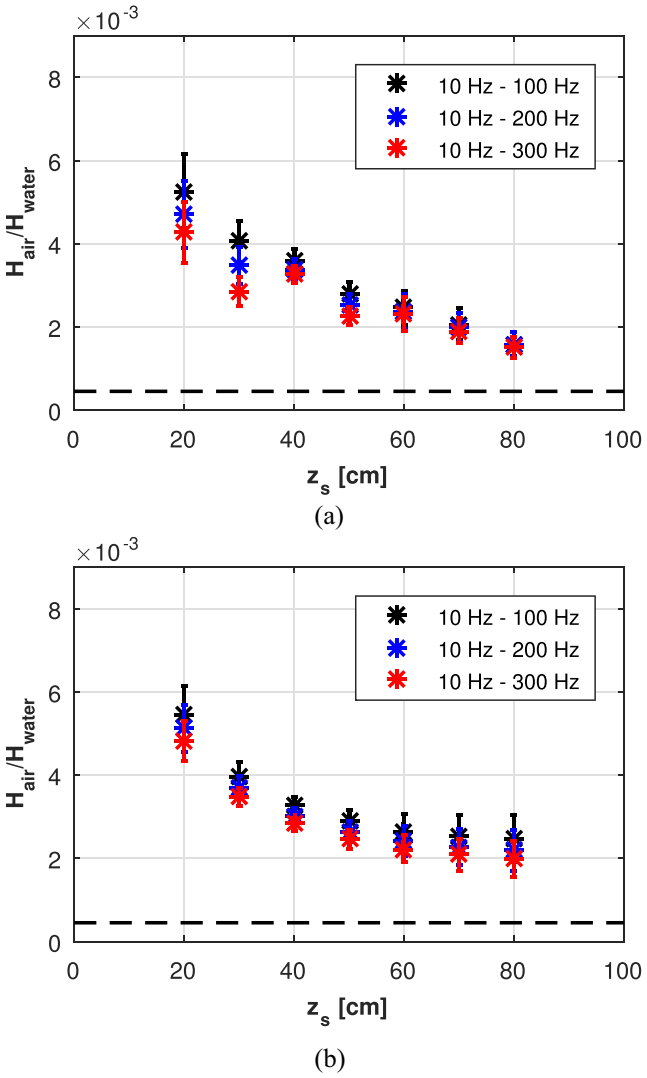

Figure 11. (a) Measured amplitude ratio for different source depths according to experiment A1. The amplitudes are corrected for geometrical spreading. The ratios are shown for different bandpass filters. The dashed line shows T_{pp}. (b) Modelled amplitude ratios for the same experiment.

they are already difficult to identify. The results from the homogeneous model differ most from the other two which is caused by the reflected signal from the interface itself. Therefore, the results from the homogeneous model could be used to separate the incident and reflected waves.

There are some drawbacks in the modelling that should be mentioned. The implemented source signatures are not recorded exactly at the source position and might be already influenced by the experimental setup itself. In addition, the metal frame above the water surface (Fig. 3a) is not taken into account in the model due to complexity. This could especially lead to deviations between modelled and measured results for the experiment where the source is placed in air.

5 RESULTS

The results from the transmission experiments in the water tank are compared with the modelled results to investigate a potential impact of the transmitted signal on source depth and frequency.

5.1 Experiment A: source in water

For a rough estimation of the transmission coefficient we compute the ratio between the mean maximum amplitude of all hydrophones in air H_{air} to those in water H_{water} as a function of the source depth z_s as

$$\frac{H_{air}}{H_{water}}(z_s) = \frac{1}{M}\left(\sum_{i}^{3}\sum_{j}^{3}\frac{A_{max}(Hi)}{A_{max}(Hj)}\frac{r_i}{r_j}\right), \quad (11)$$

where the total number of combinations is $M = i \cdot j$, r_i and r_j denote the source receiver distance for each individual hydrophone. The indices $i = 1, 2, 3$ and $j = 4, 5, 6$ denoted the hydrophones in air and water, respectively (Fig. 4). The multiplication by r_i/r_j corrects for geometrical spreading. The linear assumption is found to be the best choice by comparing measured amplitudes at all hydrophones located in air after correction. The results for different source depths z_s are illustrated in Fig. 11(a). The error bars indicate the standard deviation calculated from all ratios of each depth. The ratio is computed for three different frequency bands. Frequencies below 10 Hz are filtered out as the signal-to-noise ratio is too small for these low

frequencies. The modelled results for the same acquisition geometry and frequency bands are shown in Fig. 11(b). The modelled results agree well with the measured data, indicating the same trend and almost the same values for the ratio H_{air}/H_{water}. The deviations could be due to measuring inaccuracies or from the modelling as discussed in the Section 4.

First, we note that the measured transmitted signal is 3 to 10 times higher than the expected theoretical value T_{pp} for plane waves. The plane wave transmission coefficient is computed using eq. (2) with a density and velocity of $\rho_2 = 1.25\,\mathrm{kg\,m^{-3}}$ and $c_2 = 340\,\mathrm{m\,s^{-1}}$ in air and $\rho_1 = 1000\,\mathrm{kg\,m^{-3}}$ and $c_1 = 1500\,\mathrm{m\,s^{-1}}$ in water, respectively. We assume a vertical incident angle ($\theta = 0$) as the receivers are directly above the source. In addition, more signal is transmitted into the air when the source is closer to the interface. This general trend agrees with the theory of a spherical wave transmission response (Fig. 2). It should be mentioned that more signal seems to be transmitted for lower frequencies (Fig. 11a, black). However, these differences are small and within the error range of our measurements and hence it could not be verified with this data. The trend of increased transmission for lower frequencies could be better observed in the modelled data (Fig. 11b).

In experiment A2 the source depth is constant and the hydrophones H1, H2 and H3 (Fig. 4) are moved to different offsets to investigate the impact of the incident angle on the transmitted signal. The ratio is computed in the same way as before using eq. (11) but for a constant source depth and varying angles θ. The results are illustrated in Fig. 12(a). The modelled results for the same acquisition geometry and frequency bands are shown in Fig. 12(b). There is a good fit between the measured and modelled data, while the modelled H_{air}/H_{water} ratios are slightly lower than the measured values.

The results reveal a constant transmission until an angle of approximately $\theta = 45^\circ$. For larger angles, the ratio decreases similar to the trend of a plane wave transmission coefficient. However, the theoretical T_{pp} predicts a relative decrease of 50 per cent for the transmitted signal at 60° compared to 0°. The decrease of the measured and modelled ratios is not as strong as the one predicted by the plane wave transmission coefficient. It should be mentioned that there is a small deviation between the amplitude ratios in Figs 11(a) and 12(a) at zero-offset and a source depth of $z_s = 0.3$ m, although they should be the same. This is due to the fact that both values are computed from different tests.

It has to be noted that both tests reveal a higher ratio than expected for the plane wave transmission coefficient what could be an indication for the impact of the spherical wave front.

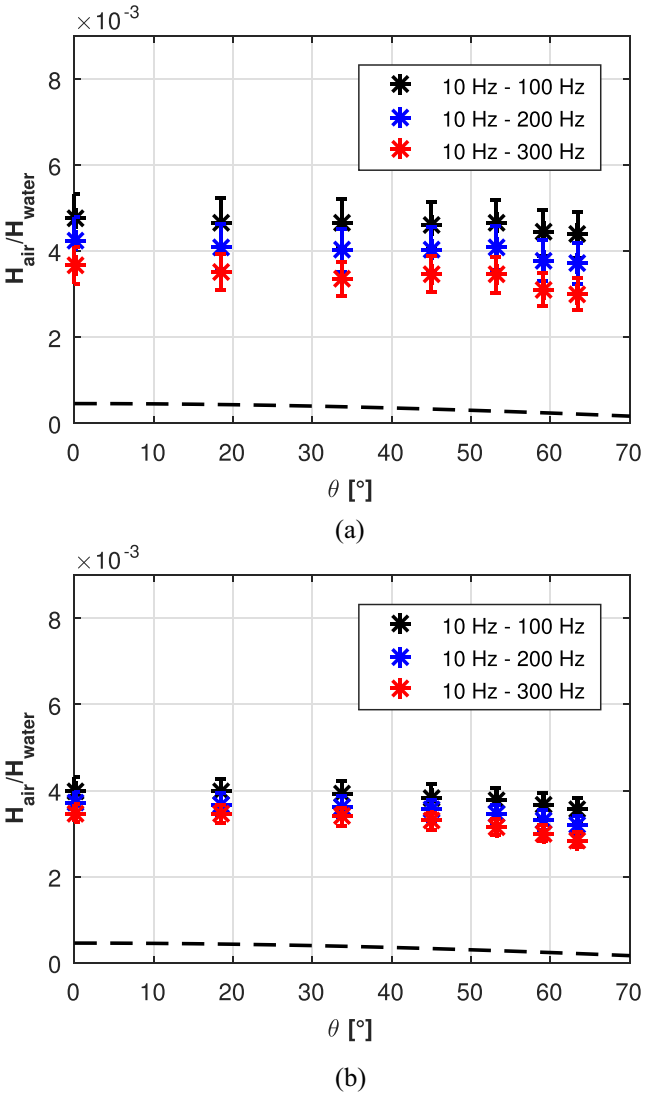

Figure 12. (a) Measured amplitude ratio for different horizontal receiver offsets in air according to experiment A2. The amplitudes are corrected for geometrical spreading. The ratios are shown for different bandpass filters. The dashed line shows T_{pp}. (b) Modelled amplitude ratios for the same experiment.

5.2 Experiment B: source in air

The results for different source elevations z_s are illustrated in Fig. 13(a). The ratio is computed using eq. (11), while it is reversed as the source is in air during this experiment. Hence, the ratio H_{water}/H_{air} is calculated for three different frequency bands. The modelled results are illustrated in Fig. 13(b). A trend of increasing ratios for smaller source–interface distances can be seen in the measured and modelled data, while there is a difference between both data sets up to 0.4 in the ratio for the shallowest source elevations. It should be mentioned that the variation of the ratios between different source–interface distances is higher than the results from experiment A.

The higher ratios within the measured data could be due to side reflections from metal frames and other obstacles that are part of the construction above the tank (Fig. 3) as these are not taken into account during the modelling. The steeper increase of the ratios for small source elevations z_s compared to experiment A could be caused by the short distance of the receivers to the interface. Therefore, the interference of the down- and upgoing wavefield for the receiver in air has a bigger impact than during experiment A. In general, it should be noted that a similar behaviour in the modelled and measured data can be observed.

6 DISCUSSION

The experimental and modelling results reveal a dependency of the transmitted signal on the source–interface distance, as well as a potential dependency on frequency that might be partly explained by the spherical shape of the wave front. The reflection coefficient can be computed from the results using eqs (4) and (8). How these findings could impact marine seismic acquisition is investigated in

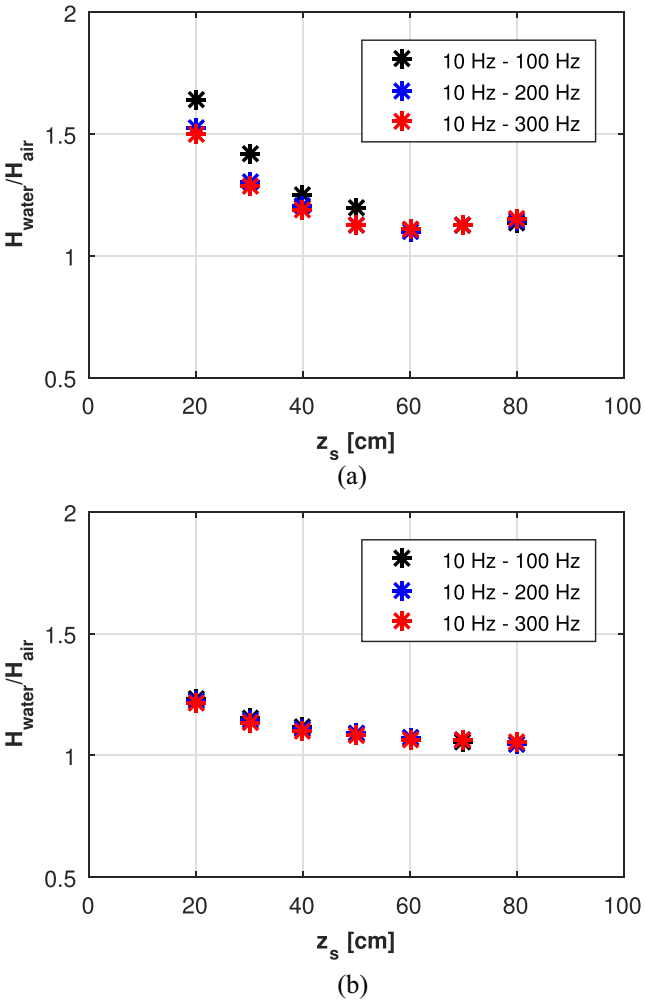

Figure 13. (a) Measured amplitude ratio for different source elevations according to experiment B. The amplitudes are corrected for geometrical spreading. The ratios are shown for different bandpass filters. (b) Modelled amplitude ratios for the same experiment.

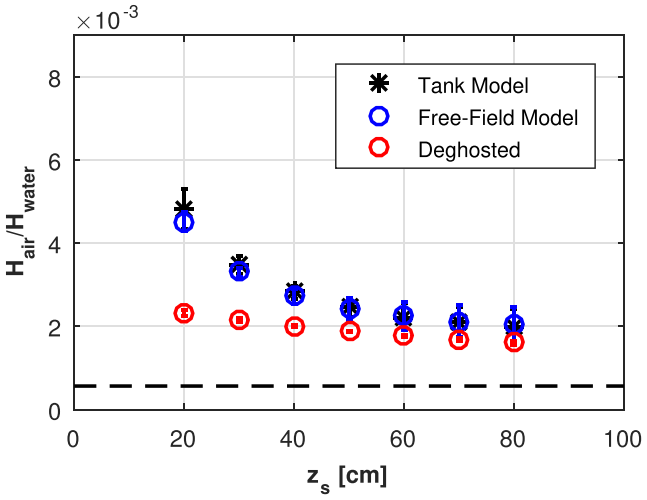

Figure 14. Results from the tank and free-field model of experiment A within frequency band of 10–100 Hz. The deghosted results are computed from the free field and homogeneous model. Theoretical plane wave transmission coefficient T_{pp} (dashed line).

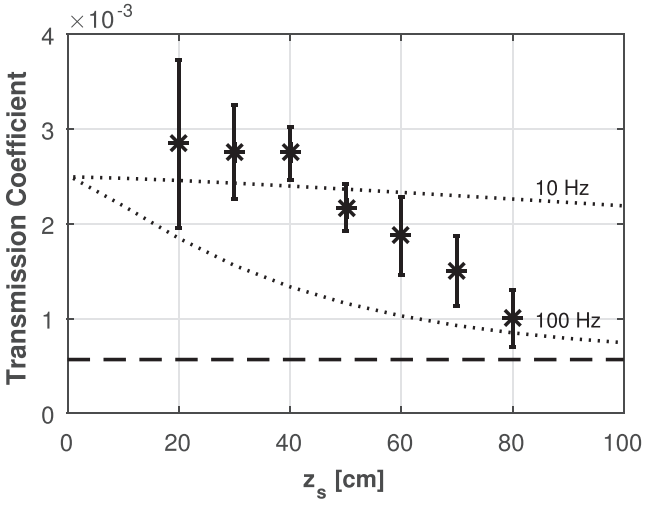

Figure 15. Measured, deghosted, results within frequency band of 10–100 Hz (asterisk), spherical wave transmission response T_{sph} for 10 and 100 Hz (dotted lines) and plane wave transmission coefficient T_{pp} (dashed line) for different source depths z_s.

more detail and hence we focus primarily on the source inside water, before we elaborate more on the reversed experiment B.

First, it should be noted that the results are influenced by the reflection from the interface itself. The amplitude recorded in water during experiment A is mainly an interference of the direct wave and the ghost reflection from the water surface. For a better quantification of the transmission and reflection coefficient, we use the results from the homogeneous model to remove the ghost effect from our data. Therefore, the ratio of the modelled amplitude from a homogeneous water medium and the modelled amplitude in air from the free-field model is computed. We denote these results as deghosted and they are illustrated in Fig. 14. This leads to a smaller transmission as the amplitude in a homogeneous model is higher than the amplitude including the interface (Fig. 10a). However, the ratio is still higher than expected for the plane wave transmission coefficient. In addition, Fig. 14 illustrates that the difference between the ratio modelled in our experimental tank setup and in the free field is small. This is a promising result as a similar trend could be expected in field applications.

For a better comparison of the experimental results to the theory of a plane wave transmission coefficient and spherical wave transmission response, we use the difference from the deghosted and free-field model (Fig. 14) to remove the ghost effect from our experimental data. The difference is subtracted from the measured ratios in experiment A1 to get a better estimation of the transmission coefficient. Then, the spherical wave transmission response T_{sph} is computed for two frequencies according to the frequency range of the measured data. The results are shown in Fig. 15 in comparison with the plane wave transmission coefficient T_{pp}. The error bars indicate the standard deviation computed from all measured ratios of each depth according to eq. (11). We note that the measured transmission coefficient is closer to the spherical wave theory than to the plane wave assumption T_{pp}, although the fit is not perfect. That the deghosted values for the shallowest sources are even higher than T_{sph}(10 Hz) could be explained by the larger deviation between the tank and free-field model for the shallower depth (Fig. 14). Further differences could be due to inaccuracies of the measured data or the deghosting method which is based on modelled results. The maximum increase of the spherical transmission response is five times

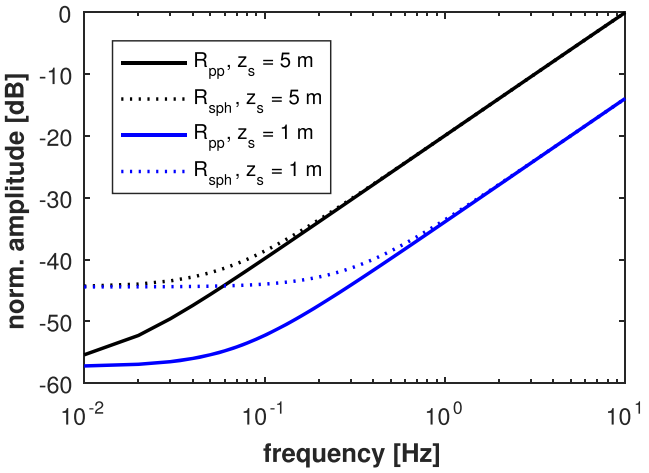

Figure 16. Comparison of ghost functions G using the plane wave (R_{pp}) and spherical wave (R_{sph}) reflection assuming two different source depths z_s. The spectra are normalized to the maximum value within the displayed frequency range.

that of the plane wave coefficient for source depths approaching the water–air interface.

It could be concluded from the results that the spherical wave transmission response has a better fit to the observations which should be the same for the reflection. However, the difference to the plane wave coefficient is small. To illustrate how different reflection coefficients could impact the frequency content in marine seismic acquisition regarding the source signal, we assume linear superposition of the downgoing and surface-reflected pressure. Then the frequency spectrum of the source ghost could be computed as

$$G = 1 + R\mathrm{e}^{(i\omega 2z_s\cos(\theta)/c_1)} \tag{12}$$

for vertical incidence ($\theta = 0^\circ$) and two different source depths z_s. The reflection coefficient R is replaced by R_{pp} and R_{sph}, respectively, where the coefficients are similar to those plotted in Fig. 2. The normalized spectra are shown in Fig. 16. The difference between both assumptions is small and barely visible for frequencies above 1 Hz. For the deep source, at 5 m depth, the difference is notable for frequencies below 0.1 Hz, with an increase of 3.5 dB for R_{sph} at 0.05 Hz compared to R_{pp}. The impact on the shallower source, at 1 m depth, could be already recognized below 1 Hz, with an increase of 5 dB for R_{sph} at 0.2 Hz. Following this example, the difference between conventional calculations of the far-field ghost assuming a constant reflection and the assumption of a spherical wave front is negligible above 0.1 Hz for typical source array depths of 5 m and deeper. Assuming a source array at 1 m depth, the difference would be negligible above 1 Hz as the difference is less than 0.5 dB in the computed far-field spectrum and less than 0.1 dB for frequencies above 2 Hz. It should be noted that these differences in the ghost effect barely vary as a function of angle for those low frequencies. If the bubble oscillation is taken into account which creates a stronger low-frequency signal for shallower depths, very shallow sources might be beneficial for frequencies below 1 Hz. This would be in agreement with findings illustrated by Landrø & Amundsen (2014). Therefore, further tests with an over-/under-configuration might be considered where a few sources are placed very shallow, about 1 m below the sea surface. The source depth might be limited by practical issues when towing sources that shallow. An investigation on the source ghost effect for different source depths is demonstrated by Haavik & Landrø (2015), however the shallowest source depths in this study is 3 m. Due to high noise levels at these frequencies caused by ocean swell, 4C ocean-bottom receivers are preferable to recognize this effect as they have a better signal-to-noise ratio at these low frequencies (Landrø *et al.* 2014; Halliday *et al.* 2015).

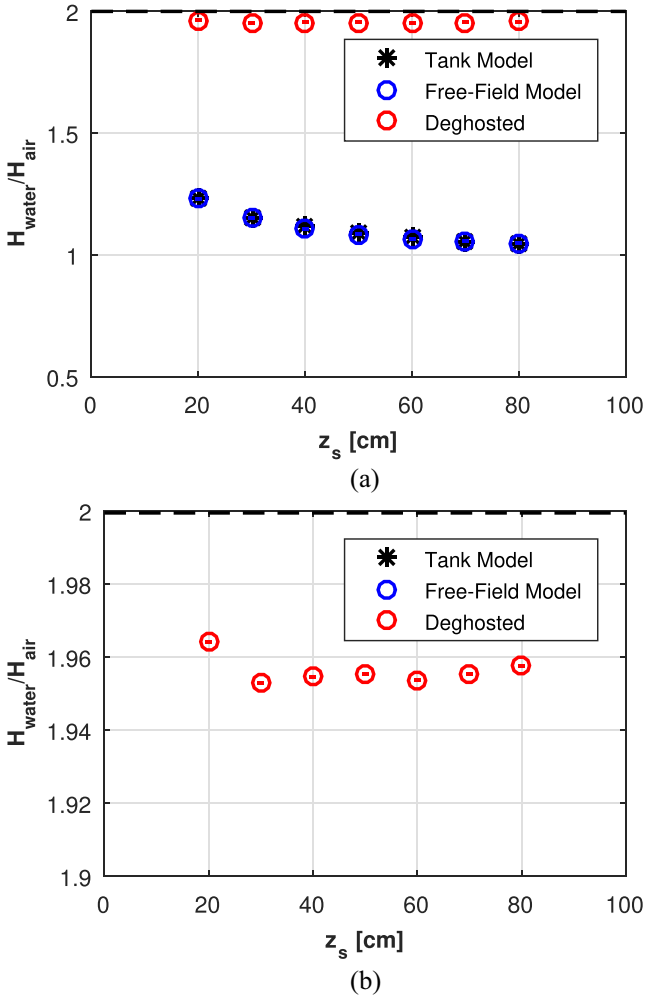

Figure 17. (a) Results from the tank and free-field model of experiment B within frequency band of 10–100 Hz. The deghosted results are computed from the free-field and homogeneous model. Theoretical plane wave transmission coefficient T_{pp} (dashed line). (b) Zoom in on plot (a).

For the modelled results from experiment B, the same deghosting method as for experiment A is performed which leads to a big change of the estimated ratio (Fig. 17a). We note again that the difference between the tank and free-field model is small. A close view on the deghosted ratio illustrates that the results are lower than the theoretical plane wave transmission coefficient (Fig. 17b). This is expected from eq. (4) if more signal is transmitted, as for a total reflection where $R = 1$, it follows $T = 2$ and for a total transmission where $R = 0$, it follows $T = 1$. The discussion is restricted on the modelled deghosted results as the deviation between modelled and measured data is too large. Therefore, the deghosting of the measured data from modelled results is not applicable for experiment B. It is difficult to conclude on a depth dependency or a quantification of the transmission coefficient from these results. However, they give some evidence that the impact of the spherical wave front might be observed as higher transmission ratios than the plane wave coefficient are observed.

It should be pointed out that all results and the theory is valid for a flat fluid–fluid interface and is not accounting for surface topography caused by weather and swell. In field applications, the effect of a rough sea surface cannot be neglected and surface topography also leads to frequency-dependent reflection. The impact on reflection and scattering from rough interfaces is discussed by many authors, which for instance is summarized by Ogilvy (1987). Whether the surface can be considered as rough or smooth can be defined by the Rayleigh parameter (Hovem 2007)

$$\chi = 2k\sigma\cos(\theta), \tag{13}$$

where σ is the mean height of the ocean waves at the sea surface and $k = (2\pi f)/v_1$ the wavenumber with frequency f and sound speed in water v_1. For values of $\chi \ll 1$ the sea surface can be assumed to be acoustically smooth. For a source in water with a frequency of $f = 1$ Hz, a mean wave height of $\sigma = 3$ m and a vertical incident acoustic wave we get $\chi = 0.0251$ according to eq. (13). As this number is much smaller than 1, a rough sea surface should have a negligible impact on the low frequency part of the ghost as the main observed difference from our results is for frequencies of 1 Hz and below. However, for frequencies above 1 Hz the weather effect could be more pronounced for these parameters following the example from Klüver & Tabti (2015). Therefore, it could be assumed that phase changes of the reflected signal from a rough sea surface might be mainly caused by the surface topography for frequencies above 1 or 2 Hz, while the phase changes for frequencies below 1 Hz could be mainly due to the spherical wave front. This simple assumption depends on the roughness of the sea surface and could change for different sea states. When the source is located in air, the transmission from air into water is more influenced by the same surface roughness as the wavenumber k is larger in air due a lower sound velocity. This leads to a Rayleigh parameter of $\chi = 0.1109$ for $f = 1$ Hz, $\sigma = 3$ m and $v_2 = 340$ m s^{-1}. Therefore, a small surface topography could lead to an increased transmission from air to water (Lubard & Hurdle 1976).

Furthermore, two other effects acting on the transmission should be discussed which were mentioned in the introduction. First, there could be an increased transmission from water to air due to the evanescent part of the wavefield as discussed by Godin (2008) and McDonald & Calvo (2007). Following the derivation of McDonald & Calvo (2007), a monopole point source that approaches $kz_s \to 0$ radiates up to 1.1 per cent of the power, that would be radiated into the unbounded medium, into air, where k is the wavenumber and z_s the source depth. For a source approaching $kz_s \to \infty$ the radiated power into air relative to that radiated into unbounded water would be 0.028 per cent and hence is much lower compared to a source close to the interface ($kz_s \to 0$). For our experiments, the range of kz_s is roughly between 0.01 and 1, and therefore this effect might influence the results. The experimental kz_s range would lead to a radiated power that is 35 times higher compared to the value in unbounded water for $kz_s = 0.01$. For $kz_s = 1$ the value should be 1.5 times higher. It should be mentioned that McDonald & Calvo (2007) describe the radiated power while we estimate the transmitted signal from peak pressure measurements. We can compare our measurements to the results of Calvo *et al.* (2013) who also evaluate pressure measurements corresponding to the same theory. They obtain similar results in the range around $kz_s = 0.1$, whereas for values approaching $kz_s = 0.01$ they achieve higher transmitted values than the results presented here. Hence, it should be noted that an increased transmission due to evanescent waves might partly influence the achieved measurements. However, the results also fit with the theoretical spherical wave reflection response and the different ghost function (Fig. 16) can still be expected. It should be mentioned that the enhanced transmission might be an explanation why we hear air guns during marine seismic acquisition louder than expected while a sufficient amount could also be transmitted through the hull of the seismic vessel.

Second, the physical interaction of the source and interface could lead to changes of the source signature and would have an impact on the measured data in air and water. The limit within interaction between the cavity and the interface happens is $z_s < 3r_{cav}$, where r_{cav} is the maximum radius of the cavity (Chahine 1977). The minimum source depths within our experiments is $z_s = 0.2$ m. We can estimate the cavity radius from the collapse time τ of the measured data as (Rayleigh 1917)

$$\tau = 0.915 r_{cav}\sqrt{\frac{\rho_w}{p_0}}, \tag{14}$$

where ρ_w is the water density, p_0 the hydrostatic pressure and 0.915 is an exact number derived from gamma functions by Rayleigh (1917). With a measured collapse time of $2\tau = 0.03$ s from the shallowest source depths a cavity radius of $r_{cav} = 0.023$ m is estimated similar to the approach by Safar (1986). This is more than eight times the source depths $z_s = 0.2$ m and therefore we consider the effect of source–interface interaction as negligible for our experiments. Within seismic acquisition where the bubble of the air gun is much larger than the cavity in our experiments, this effect has to be considered. It should also be mentioned that further phenomena as cavitation and the shot effect (Loveridge 1985) are expected during air gun operations at shallow source depths.

7 CONCLUSION

The experimental results indicate an increased transmission for smaller distances between the source and water–air interface. The measured data fits to the model and theory of a spherical wave reflection response that reveals a decreased reflection from the sea surface for shallow sources and large wavelength relative to the source–interface distance. It should be noted that the increased transmission from water to air might be also partly explained by the evanescent waves in water that could convert to homogeneous waves in air for certain wavenumbers. However, considering the results together with the model and theory, very shallow seismic sources seem to be beneficial for an enhanced very low frequency signal in marine seismic acquisition. As the highest noise levels in marine seismic acquisition are also in the low-frequency range below 2 Hz, it depends on the source strength and low-frequency noise level at the receivers whether the difference between the plane and spherical wave assumption can be recognized or not.

ACKNOWLEDGEMENTS

We acknowledge the European Union's Horizon 2020 research and innovation programme under the Marie Skłodowska-Curie grant agreement No. 641943 for the funding of Daniel Wehner's PhD project within WAVES. We like to acknowledge the technical team at IGP for their support to the experimental setup. ML acknowledges financial support from the Norwegian Research Council. We thank Joshua (Shuki) Ronen and an unknown reviewer for their valuable comments which improved this paper.

REFERENCES

Aki, K. & Richards, P.G., 2002. *Quantitative Seismology,* Universtiy Science Books.

Amundsen, L., Westerdahl, H., Pederson, A.S., Thompson, M. & Landrø, M., 2017. On firing an air gun very shallow, *Geophysics,* **82**(3), A25–A29.

Barker, D. & Landrø, M., 2012. Simple expression for the bubble-time period of two clustered air guns, *Geophysics,* **77,** A1–A3.

Blake, J.R. & Gibson, D.C., 1981. Growth and collapse of a vapour cavity near a free surface, *J. Fluid Mech.,* **111,** 123–140.

Brekhovskikh, L.M. & Lysanov, Y.P., 1991. *Fundamentals of Ocean Acoustics,* Springer.

Calvo, D.C., Nicholas, M. & Orris, G.J., 2013. Experimental verification of enhanced sound transmission from water to air at low frequencies, *J. acoust. Soc. Am.,* **134**(5), 3403–3408.

Chahine, G.L., 1977. Interaction between an oscillating bubble and a free surface, *J. Fluids Eng.,* **99**(4), 709–176.

Courant, R., Friedrichs, K. & Lewy, H., 1928. Über die partiellen Differenzengleichungen der mathematischen Physik, *Math. Ann.,* **100**(1), 32–74.

Deng, Y., Tao, J. & Qiu, X., 2012. Sound radiation into air by a point source moving underwater, *J. Sound Vib.,* **331,** 4481–4487.

Giles, B.F. & Johnston, R.C., 1973. System approach to air-gun design, *Geophys. Prospect.,* **21,** 77–101.

Glushkov, E.V., Glushkov, N.V. & Godin, O.A., 2013. The effect of anomalous transparency of the water-air interface for a volumetric sound source, *Acoust. Phys.,* **59**(1), 6–15.

Godin, O.A., 2006. Anomalous transparency of water–air interface for low-frequency sound, *Phys. Rev. Lett.,* **97**(16), 164301–1-164301-4.

Godin, O.A., 2008. Sound transmission through water–air interfaces: new insights into an old problem, *Contemp. Phys.,* **49**(2), 105–123.

Haavik, K.E. & Landrø, M., 2015. Variable source depth acquisition for improved marine broadband seismic data, *Geophysics,* **80**(3), A69–A73.

Halliday, D., Laws, R. & Garden, M., 2015. Signal and noise in a shallow-water ocean-bottom cable survey, in *85th Annual International Meeting, SEG, Expanded Abstracts,* New Orleans, LA, USA, pp. 120–124.

Hovem, J.M., 2007. *Marine Acoustics, The Physics of Sound in Underwater Environments,* Peninsula Publishing.

Hudimac, A.A., 1957. Ray theory solution for the sound intensity in water due to a point source above it, *J. acoust. Soc. Am.,* **29**(8), 916–917.

Huygens, C., 1690. *Treatise on Light,* University of Chicago Press [translated by Thompson SP].

Jensen, F.B., Kuperman, W.A., Porter, M.B. & Schmidt, H., 2011. *Computational Ocean Acoustics,* Springer.

Kinsler, L.E., Frey, A.R., Coppens, A.B. & Sanders, J.V., 1962. *Fundamentals of Acoustics,* 4th edn, John Wiley & Sons, Inc.

Klüver, T. & Tabti, H., 2015. Derivation of statistical sea-surface information from dual-sensor towed streamer data, in *77th Conference & Exhibition, EAGE, Expanded Abstracts,* Madrid, Spain, doi:10.3997/2214-4609.201413187.

Kryvohuz, M. & Campman, X., 2017. Source-side up-down wavefield separation using dual NFHs, in *79th Conference & Exhibition, EAGE, Expanded Abstracts,* Paris, France, pp. TuA406.

Landrø, M. & Amundsen, L., 2014. Is it optimal to tow air guns shallow to enhance low frequencies? *Geophysics,* **79**(3), A13–A18.

Landrø, M., Zaalberg-Metselaar, G., Owren, B. & Vaage, S., 1993. Modeling of water-gun signatures, *Geophysics,* **58**(1), 101–109.

Landrø, M., Haavik, K.E. & Amundsen, L., 2014. Using geophone components to obtain ultralow frequency seismic signals at long offsets, in *84th Annual International Meeting, SEG, Expanded Abstracts,* Denver, CO, USA, pp. 233–237.

Li, J., Wang, S., Tao, Y., Dong, C. & Tang, G., 2017a. A novel expression of the spherical-wave reflection coefficient at a plane interface, *Geophys. J. Int.,* **211,** 700–717.

Li, J., Wang, S., Wang, J., Dong, C. & Yuan, S., 2017b. Frequency-dependent spherical-wave reflection in acoustic media: analysis and inversion, *Pure appl. Geophys.,* **174,** 1759–1778.

Loveridge, M.M., 1985. Marine seismic source signatures, directivity and the ghost, *PhD thesis*, University of Oxford, Oxford, UK.

Lubard, S.C. & Hurdle, P.M., 1976. Experimental investigation of acoustic transmission from air into a rough ocean, *J. acoust. Soc. Am.,* **60**(5), 1048–1052.

McDonald, B.E. & Calvo, D.C., 2007. Enhanced sound transmission from water to air at low frequencies, *J. acoust. Soc. Am.,* **122**(6), 3159–3161.

Ogilvy, J.A., 1987. Wave scattering from rough surfaces, *Rep. Prog. Phys.,* **50**(12), 1553–1608.

Rayleigh, O.M., 1917. On the pressure developed in a liquid during the collapse of spherical cavity, *Philos. Mag.,* **34,** 94–98.

Safar, M.H., 1986. A simple method for determining the S80 water gun depth, *Geophysics,* **51**(2), 424–426.

Strandenes, S. & Vaage, S., 1992. Signatures from clustered airguns, *First Break,* **10**(8), 305–312.

Ursenbach, C.P. & Haase, A.B., 2006. AVO modeling of monochromatic spherical waves: comparison to band-limited waves, *CREWES Res. Rep.,* **18,** 1–12.

Voloshchenko, A.P. & Tarasov, S.P., 2013. Effect of anomalous transparency of a liquid–gas interface for sound waves, *Acoust. Phys.,* **59**(2), 163–169.

Wang, Q.X., Yeo, K.S., Khoo, B.C. & Lam, K.Y., 1996. Strong interaction between a buoyancy bubble and a free surface, *Theor. Comput. Fluid Dyn.,* **8,** 73–88.

Yan, B.P., Wang, S.X., Yuan, S.Y., Ji, Y.Z. & Tao, Y.H., 2017. Frequency-dependent reflection coefficient of spherical wave in acoustic medium, in *79th EAGE Conference & Exhibition,* Paris, France, pp. Tu P1 10.

Young, R.W., 1973. Sound pressure in water from a source in air and vice versa, *J. acoust. Soc. Am.,* **53**(6), 1708–1716.